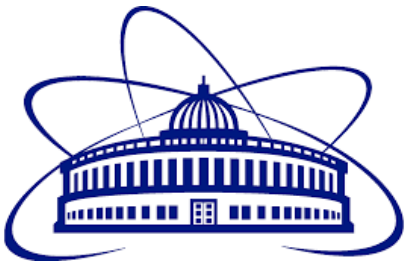

JOINT INSTITUTE FOR NUCLEAR RESEARCH
Bogoliubov Laboratory of Theoretical Physics

FINAL REPORT ON THE

START PROGRAMM

Method NRF and program TALYS for studying low-energy photonuclear reactions

Supervisor:
Dr. Valentin Olegovich Nesterenko

Student:
Wang Yanzhao, China
Tomsk Polytechnic University

Participation period:
October 12 - November 22,
Summer Session 2025

Dubna, 2025

Contents

Abstract

Photonuclear reactions at low energies provide crucial insights into nuclear structure, giant dipole resonances, and astrophysical nucleosynthesis processes. This project investigates the nuclear resonance fluorescence (NRF) method for probing nuclear excitations and employs the TALYS nuclear reaction code to model photonuclear processes on molybdenum isotopes.

The fundamental principles of the NRF method are described, and research results from several related laboratories are listed. We derive the angular distribution for 0-1-0 spin sequences in NRF and discuss techniques to distinguish magnetic (M) and electric (E) multipolarities.

A brief introduction to software package TALYS are presented. Its framework combines energy level density and photon intensity functions with various nuclear models. We use different TALYS models to simulate the cross-section of the (γ, p) and (γ, n) channel. Calculated results are compared with experimental data from the IAEA nuclear database, demonstrating good agreement in the energy range of 10-23 MeV. This study underscores the synergy between experimental NRF techniques and theoretical modeling for advancing low-energy photonuclear physics research.

1 Introduction

Low-energy photonuclear reactions, induced by gamma rays in the energy regime below the pion production threshold (typically 1-40 MeV), serve as a powerful probe for understanding nuclear excitations, particularly the giant dipole resonance (GDR) [1]. These reactions offer distinct advantages over nucleon-induced processes due to the well-characterized electromagnetic interaction, enabling precise studies of nuclear structure, decay modes, and multipolarity assignments. In astrophysics, photonuclear pathways play a pivotal role in the synthesis of p-nuclei, through mechanisms like the γ-process, where discrepancies between observed abundances and model predictions persist [2].

NRF emerges as a key experimental technique in this domain, leveraging quasi-monochromatic polarized gamma beams to excite nuclear states and observe resonant scattering. By analyzing angular distributions, NRF allows determination of excitation energies, multipolarity, parities, and cross sections, providing benchmarks for theoretical models. Complementing these experiments, computational tools like TALYS [3] integrate advanced nuclear reaction theories—including the optical model, compound nucleus decay, pre-equilibrium processes, and photon strength functions—to simulate cross sections and yields across a wide range of energies and isotopes.

This report explores the principles of NRF, including derivations for specific angular distributions and multipolarity discrimination, and details the application of TALYS for modeling photonuclear reactions on stable molybdenum isotopes [4]. Focusing on the ^{92}Mo(γ, n)^{92}Mo channel, we compare TALYS predictions with experimental data from bremsstrahlung-induced activations. Through this integrated approach, we aim to bridge experimental observations with theoretical simulations.

2 Project goals

The primary aim of this project is to advance the understanding of low-energy photonuclear physics through a combination of experimental techniques and theoretical modeling, with a specific focus on molybdenum isotopes.

The specific objectives are:

1. Investigating the fundamental principles of NRF, including its experimental apparatus for detecting nuclear transitions. The goal is to demonstrate how NRF serves as a precise tool for probing nuclear structure, excitation energies, and transition strengths, providing benchmarks for theoretical predictions.

2. Gain a comprehensive understanding of the TALYS nuclear reaction code [4]. This objective includes exploring how TALYS incorporates nuclear structure inputs, with an emphasis on its applicability to low-energy photonuclear reactions on stable isotopes.

3. Using TALYS to calculate the cross section for the ^{92}Mo(γ, p)^{91m}Nb reaction in the energy range of 10-23 MeV. Compare the simulated results with experimental data from the IAEA photonuclear database, evaluating the impact of model parameters. This validation aims to refine theoretical descriptions of photoproton reactions.

The project bridges experimental observations with computational modeling to enhance nuclear data accuracy. The outcomes are expected to support applications in nuclear structure, while highlighting areas for future model improvements.

3 Nuclear resonance fluorescence

Nuclear resonance fluorescence is referred to as real-photon scattering. It is a widely used method to investigate properties of excited low-spin states in atomic nuclei [5, 6]. On one hand, nuclear levels are characterized by their spin (J) and parity (π) quantum numbers, respectively. On the other hand, the lifetime τ of an excited state is usually one of the common and important observables in nuclear physics experiments and is inversely proportional to the natural line width Γ.

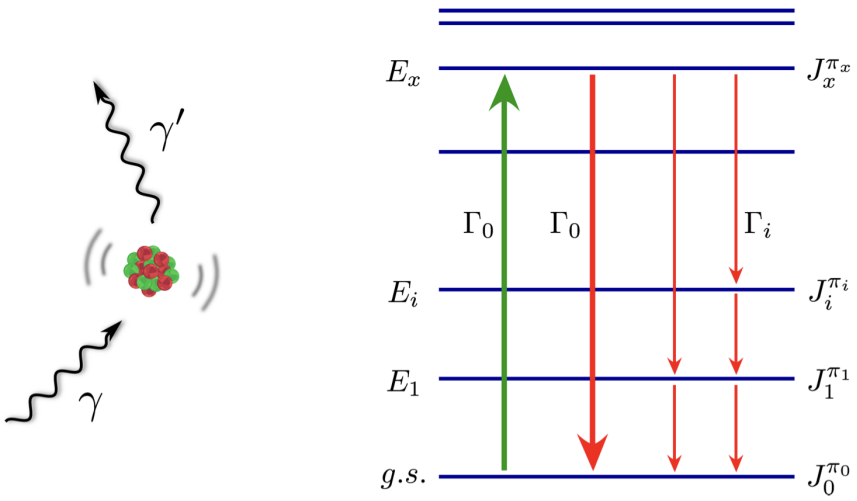

Figure 1: Schematic overview of the NRF method. By resonant photoabsorption the nucleus is excited from the ground state with spin-parity quantum numbers J_0^π to an excited state with spin-parity J_x^π. The corresponding excitation probability is proportional to the ground-state transition width Γ_0. Subsequently, the nucleus can either decay directly back to the ground state (thick red arrow) or cascade via intermediate levels (thin red arrows). The transition width Γ_i is directly linked to the probability for the transition between two states J_x^π and J_i^π.

In the (γ, γ') reaction, a real photon is resonantly absorbed by the nucleus, which subsequently de-excites via the emission of another photon. This process is schematically illustrated in Fig.1. In this manner, the nucleus is excited from the ground state with spin-parity quantum number J_0^π to a state with J_x^π and excitation energy E_x. The corresponding excitation probability is expressed by the ground-state transition width Γ_0. In the de-excitation channel, usually two different outcomes are considered. Either the nucleus releases its total

excitation energy in one transition and decays directly back to the ground state or it emits the energy step-by-step via cascade transitions. The ground-state transition is commonly connected to the term elastic. In a classical picture, however, this term is not correct, since the emitted photon is not the same as the absorbed one. In analogy to that, the transition from a photo-excited state to a lower-lying level other than the ground state is denoted as inelastic [7]. In this case, the transition probabilities are connected to the transition widths Γ_i (see Fig.1).

The excitation and the de-excitation process is dominated by the electromagnetic interaction, which is one of the best understood phenomena in physics. Thus, the extraction of intrinsic properties of individual excited levels accessible from observables can be performed in a model-independent way. Such quantities are, e.g., excitation energies, spin and parity quantum numbers, as well as transition strengths. The corresponding theoretical framework has been developed as early as 1937 by Bethe and Placzek and has been comprehensively adapted for the particular case of NRF in the review of Metzger in 1959 [1]. Recent reviews and progress of experimental nuclear structure studies using the NRF technique can be found in Ref. [8–11].

The photon scattering cross section integrated over a single resonance, is given by:

$$\frac{d\sigma(\gamma,\gamma')}{d\Omega} = \left(\frac{2J+1}{2J_0+1}\right)\frac{\pi\hbar^2c^2}{E_x^2}\frac{\Gamma_0\Gamma_i}{\Gamma}\frac{W(\theta,\phi)}{4\pi}, \tag{1}$$

Where J_0 and J are the spins of the ground and excited state, respectively. Γ_0, Γ_i, and Γ represent the ground state decay width, the decay width to an intermediate level, and the total decay width of the considered excited state. E_x is the excitation energy of the level and $W(\theta,\phi)$ the angular distribution of the emitted radiation. The scattering angle θ is the angle between the incoming and scattered photon, while the azimuthal angle ϕ is defined by the angle between the scattering and the polarization plane. For unpolarized photon beam, the angular distribution becomes dependent only on θ and can be described by a sum of Legendre polynomials, depending on the multipolarity of the transition [12–14].

To obtain the form of the angular distribution, we need to start with the orientation parameters.The orientation parameter $B_\nu(\gamma_0)$ for unpolarized photons is given by:

$$B_\nu(\gamma_0) = (2J_1+1)^{1/2}\cdot\sum_{m_J}(-1)^{J_1+m_J}\cdot\langle J_1 - m_J J_1 m_J|\nu 0\rangle\cdot P(m_J). \tag{2}$$

Here, J_1 is the spin of the oriented state, m_J are the magnetic substates, $P(m_J)$ is the relative population of the magnetic substates, and $\langle\cdot|\cdot\rangle$ denotes the Clebsch-Gordan coefficient.

For unpolarized photons, it can also be expressed as:

$$B_\nu(\gamma_0) = \frac{1}{1+\delta_0^2} \cdot [F_\nu(LLJ_0J_1) - 2\delta_0 \cdot F_\nu(LL'J_0J_1) + \delta_0^2 \cdot F_\nu(L'L'J_0J_1)]. \tag{3}$$

The parameters include the mixing ratio $\delta_0 = \gamma(\lambda'L')/\gamma(\lambda L)$, where $\gamma(\lambda L)$ is the reduced matrix element for the λL transition, and F_ν are the F-coefficients.

The ordinary F-coefficient is:

$$F_\nu(LL'J_0J_1) = (-1)^{J_0+J_1+1} \cdot [(2\nu+1)(2L+1)(2L'+1)(2J_1+1)]^{1/2} \times \\ \times \begin{pmatrix} L & L' & \nu \\ 1 & -1 & 0 \end{pmatrix} \begin{Bmatrix} L & L' & \nu \\ J_1 & J_1 & J_0 \end{Bmatrix}. \tag{4}$$

This involves 3j-symbols and 6j-symbols, with spins J_0, J_1 and multipoles L, L'.

The angular distribution for polarized photons is:

$$W(\vartheta,\phi) = \sum_{\nu=0,2,4} B_\nu(\vec{\gamma_0}) A_\nu(\gamma_1) P_\nu(\cos\vartheta) + \\ + B_\nu(\vec{\gamma_0})(-1)^{\sigma(\lambda')} \kappa_\nu(LL') \cdot A_\nu(\gamma_1) P_\nu^{(2)}(\cos\vartheta)\cos(2\phi). \tag{5}$$

Here, $W(\vartheta)$ is the unpolarized distribution, $P_\nu^{(2)}$ is the unnormalized associated Legendre function, ϕ is the azimuthal angle, $\sigma(\lambda')$ is 0 for electric and 1 for magnetic transitions, and $\kappa_\nu(LL')$ is a coefficient.

The linear-polarization orientation parameter is:

$$B'_\nu(\vec{\gamma_0}) = (-1)^{\sigma(\lambda)} \frac{1}{1+\delta_0^2} \cdot [\kappa_\nu(LL) \cdot F_\nu(LLJ_0J_1) + \\ + 2\delta_0 \cdot \kappa_\nu(LL) \cdot F_\nu(LL'J_0J_1) - \delta_0^2 \cdot \kappa_\nu(LL) \cdot F_\nu(L'L'J_0J_1)]. \tag{6}$$

This modifies B_ν for polarization, with parameters as above.

The coefficient κ_ν is:

$$\kappa_\nu(LL') = -\left[\frac{(\nu-2)!}{(\nu+2)!}\right]^{1/2} \cdot \frac{C(LL'\nu,11)}{C(LL'\nu,1-1)}. \tag{7}$$

Here, C are Clebsch-Gordan coefficients.

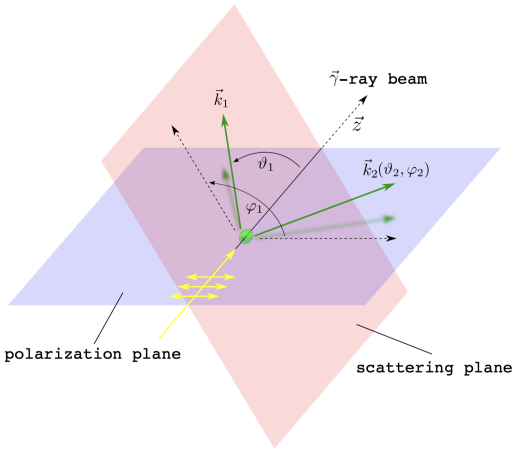

Figure 2: Illustration of the coordinate system for the $\gamma - \gamma'$ correlation of two photons (green arrows) emitted in the decay of a nuclear level, that is excited via a linearly polarized photon beam (yellow arrow). A more detailed description is given in the text.

For the 0-1-0 sequence with E1 transitions:

$$W(\vartheta, \phi) = \frac{3}{4}[1 + \cos^2\vartheta + \pi_1 \cdot \cos(2\phi) \cdot \sin^2\vartheta]. \tag{8}$$

π_1 is the parity of the excited state.
For the 0-2-0 sequence with E2 transitions:

$$W(\vartheta, \phi) = \frac{5}{8}[2 + \cos(2\vartheta) + \cos(4\vartheta) - (1 + 2\cos(2\vartheta)) \cdot 2\cos(2\phi)\sin^2\vartheta]. \tag{9}$$

Measuring $W(\theta)$ enables the determination of the multipolarity of the transition. For even-even nuclei with ground state spin $J_0 = 0$ it is sufficient to measure only under the optimal angles of 90° and 127°. The ratio $W(90°)/W(127°)$ amounts to 0.73 for dipole transitions and 2.28 for quadrupole transitions. The latter value is slightly changed to 2.14 when the solid angles of the detectors are taken into account.

For elastic transitions, where the excited state decays back to the ground state ($\Gamma_i = \Gamma_0$), the observed cross section is proportional to Γ_0^2/Γ. If the total decay width is known, or assumed to equal the ground state transition width ($\Gamma = \Gamma_0$), the reduced transition probability $B(\pi, L) \uparrow$ for the transition with parity π and multipolarity L is extracted by means of the relation:

$$\Gamma_0 = \frac{8\pi(L+1)}{L[(2L+1)!!]^2}\left(\frac{E_x}{\hbar c}\right)^{2L+1}\frac{2J_0+1}{2J+1}B(\pi, L)\uparrow . \tag{10}$$

Parities were determined using linearly polarized photons in the entrance channel and by measuring the azimuthal asymmetry of the scattered photons. The asymmetry is measured for photons scattered parallel ($\phi = 0°, 180°$) and perpendicular ($\phi = 90°, 270°$) to the polarization plane under a scattering angle $\theta = 90°$. The analyzing power $\Sigma(\theta)$ for this reaction is defined as the normalized difference of the angular distributions perpendicular ($\perp$) and parallel ($\parallel$) to the polarization plane:

$$\Sigma(\theta) = \frac{W(\theta, \phi = \pi/2) - W(\theta, \phi = 0)}{W(\theta, \phi = \pi/2) + W(\theta, \phi = 0)}. \tag{11}$$

The maximum analyzing power for $0^+ - 1^{\pi_1} - 0^+$ and $0^+ - 2^+ - 0^+$ spin cascades occurs at $\theta = 90°$ and is $+1$ for negative parity transitions (E1) and -1 for positive parity transitions (M1 and E2) [8]. For a not completely polarized incoming beam with polarization P^γ, the measured asymmetry ϵ can be represented as

$$\epsilon = \frac{N_\perp - N_\parallel}{N_\perp + N_\parallel} = P^\gamma \Sigma(\theta), \tag{12}$$

where $N_\perp$ and $N_\parallel$ are the number of counts, respectively, for the detectors perpendicular to and in the polarization plane. Comparing the measured asymmetry with the known polarization degree of the beam thus reveals the parity of the observed transition.

4 TALYS for simulating photonuclear reactions

TALYS stands as a versatile nuclear reaction simulation code, crafted by A. J. Koning, S. Hilaire, and S. Goriely to analyze and predict nuclear reactions across diverse projectiles, targets, and energies [3, 15]. By seamlessly integrating advanced nuclear structure models with various reaction mechanisms, it delivers a broad spectrum of observables, including cross sections, spectra, angular distributions, and yields. In the realm of low-energy photonuclear physics, TALYS proves particularly adept at modeling gamma-induced processes that illuminate giant dipole resonances (GDRs), astrophysical nucleosynthesis pathways, and the production of medical isotopes [4, 16, 17].

The code's applicability spans incident energies from 1 keV to 200 MeV, with extensions up to 1 GeV for certain models like optical potentials. It accommodates projectiles such as neutrons, protons, deuterons, tritons, ^{3}He, alphas, and photons, targeting nuclei from hydrogen (Z=1) to superheavy elements (Z=120) with masses A $\geq$ 2. For photonuclear reactions, TALYS effectively covers energies from reaction thresholds (around 8–10 MeV for (γ,n) or (γ,p)) to 200 MeV, encompassing the GDR region (8–40 MeV) where electromagnetic interactions prevail. It excels in forecasting photoabsorption, photoneutron, photoproton, and photofission cross sections, alongside flux-averaged yields from bremsstrahlung sources [18].

Operating TALYS involves executing Fortran-based scripts via command-line interfaces with customized input files. The latest iteration, TALYS-2.0 (released in December 2023), is accessible from the IAEA Nuclear Data Services website or its GitHub repository [19]. Installation requires a Fortran compiler like gfortran, with compilation of source files in the `talys/source` directory. A separate nuclear structure database (∼1.3 GB) must be downloaded and placed in `talys/structure/`. Users prepare input files (e.g., `input.talys`) specifying keywords for projectiles, targets, energies, models, and outputs, then run the code as `talys < input.talys > output.talys`. Sample inputs and verification scripts in the `samples/` directory facilitate testing.

The main keywords in the input file are: incident particle, energy range, target atom, and target atom mass number. In addition to these main keywords, different models can be used using different keywords, such as nuclear level density and photon radiation intensity functions.

In low-energy photonuclear reactions, such as those in the 10–23 MeV

ldmodel 1: Constant Temperature + Fermi gas model (CTM)
ldmodel 2: Back-shifted Fermi gas Model (BFM)
ldmodel 3: Generalised Superfluid Model (GSM)
ldmodel 4: Skyrme-Hartree-Fock-Bogolyubov level densities from numerical tables
ldmodel 5: Skyrme-Hartree-Fock-Bogolyubov combinatorial level densities from numerical tables
ldmodel 6: Temperature-dependent Gogny-Hartree-Fock-Bogolyubov combinatorial level densities from numerical tables
ldmodel 2 41 93: Back-shifted Fermi gas Model just for this particular nucleus

Figure 3: Keywords of model for nuclear level densities in TALYS.

strength 1 : Kopecky-Uhl generalized Lorentzian
strength 2 : Brink-Axel Lorentzian
strength 3 : Hartree-Fock BCS tables
strength 4 : Hartree-Fock-Bogoliubov tables
strength 5 : Goriely's hybrid model [50]
strength 6 : Goriely T-dependent HFB
strength 7 : T-dependent RMF
strength 8 : Gogny D1M HFB+QRPA
strength 9 : SMLO
strength 10: Skyrme HFB+QRPA

Figure 4: Keywords of models for E1 gamma-ray strength function.

range for molybdenum isotopes, TALYS employs a hybrid framework blending direct, compound, and pre-equilibrium mechanisms, prioritizing PSFs for initial gamma absorption. Treating photons as projectiles (`projectile g`), it computes absorption cross sections $\sigma_{\rm abs}$ and ensuing emissions. Core models feature PSFs modeled phenomenologically via Lorentzian forms (e.g., Kopecky-Uhl, Brink-Axel; `strength 1-2`) or microscopically through QRPA (`strength 3-10`), with defaults like SMLO (`strength 9`). Photoabsortion cross section gives $\sigma_{\rm abs} = \sigma_{\rm GDR} + \sigma_{\rm QD}$. The essential relation between the photoabsorption cross section and the upward PSF is $\sigma_{Xl}(E_\gamma) = (2l+1)\pi^2\hbar^2c^2E_\gamma^{2l-1}f^{\rightarrow}_{XL}(E_\gamma)$.

Besides TALYS, there are other codes that can be used for calculation of photonuclear reactions, such as EMPIRE, CCONE, MEND-G, GLUNF, and CoH3.

```
#
# General
#
projectile g
element mo
mass 92
energy energies 10 25 0.25  # MeV
strength 9  # SMLO PSF
isomer y  # Include isomeric states like 91mNb
channels y  # Exclusive cross sections
filechannels y  # Output (γ,p) in channels.gp
outgamma y  # PSF and photoabsorption details
best y  # Use pre-tuned parameters for (γ,p)
```

Figure 5: Input file for calculating the 92Mo(γ, *) reaction cross section (exclusive neutron emission channel) over the energy range 10-25 MeV with grid 0.25 MeV. TALYS treats photons as projectiles with projectile g, and the (γ, n) channel is computed via the SMLO model using the selected photon strength function (PSF) model via the strength keyword.

```
# header:
#   title: Mo92(g,reac) cross section
#   source: TALYS-2.0
#   format: YANDF-0.1
# target:
#   Z: 42
#   A: 92
#   nuclide: Mo92
# reaction:
#   type: (g,reac)
# datablock:
#   quantity: cross section
#   columns: 2
#   entries: 101
##       E             xs
##     [MeV]          [mb]
   5.000000E+00   3.014829E-01
   5.250000E+00   3.607563E-01
   5.500000E+00   4.318944E-01
   5.750000E+00   5.168626E-01
   6.000000E+00   6.178719E-01
   6.250000E+00   7.372415E-01
   6.500000E+00   8.771268E-01
   6.750000E+00   1.039040E+00
   7.000000E+00   1.223120E+00
   7.250000E+00   1.427206E+00
   7.500000E+00   1.646030E+00
```

Figure 6: Output file for calculation total cross section of reaction 92Mo(γ, *)

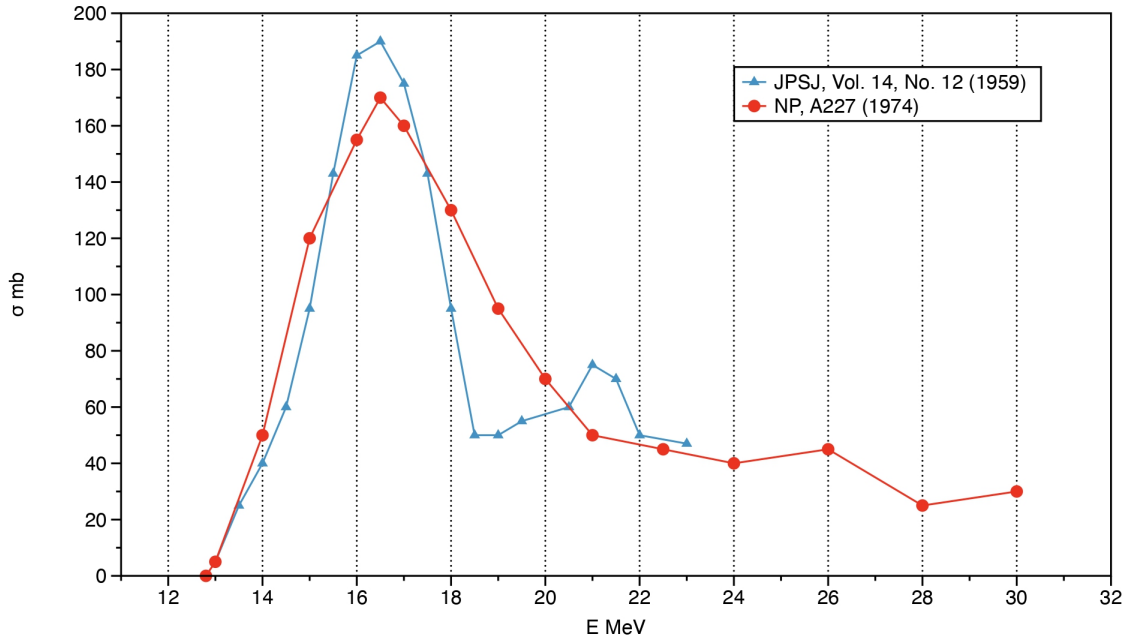

Figure 7: Photoneutron reaction experimental data, where the red dot represents cross-section $^{92}\mathrm{Mo}(\gamma,\mathrm{n})+^{92}\mathrm{Mo}(\gamma,\mathrm{np})$, and the blue triangle represents cross-section $^{92}\mathrm{Mo}(\gamma,\mathrm{n})$

5 Cross section of $^{92}\mathrm{Mo}(\gamma,\mathrm{n})^{91}\mathrm{Mo}$

The cross sections are fitted using a Lorentzian lineshape, which provides a suitable approximation for the main resonance peak. The Lorentzian form for the cross section $\sigma(E_\gamma)$ is given by:

$$\sigma(E_\gamma) = \frac{\sigma_{\max}}{1+\left(\frac{E_\gamma^2-E_0^2}{E_\gamma\Gamma}\right)^2},$$

where E_γ is the gamma-ray energy in MeV, $\sigma_{\max}$ is the peak cross section in millibarns (mb), E_0 is the resonance energy in MeV, and Γ is the full width at half maximum (FWHM) in MeV. The integrated cross section σ_{int} is computed up to $E_\gamma = 25$ MeV, approximating the integral from the neutron binding energy threshold B_n to this cutoff using the Lorentzian approximation:

$$\sigma_{\text{int}} \approx \frac{\pi}{2}\sigma_{\max}\Gamma.$$

For the $\sigma(\gamma, n)$ data, the main peak is well-defined. The approximate fit parameters are $\sigma_{\max} \approx 190$ mb, $E_0 \approx 16.5$ MeV, and $\Gamma \approx 3.0$ MeV. The fitted cross section is:

$$\sigma(\gamma, n) \approx \frac{190}{1 + \left(\frac{E_\gamma^2 - 16.5^2}{3.0 E_\gamma}\right)^2} \quad \text{(mb)}.$$

The integrated cross section up to 25 MeV, considering the rapid decline beyond 18.5 MeV, is estimated as $\sigma_{\text{int}}(\gamma, n) \approx 750$ to 850 MeV·mb.

However, in the data graph of (γ, n) exhibit complexities near the two-neutron separation energy E_{2n}. This is likely due to the inability to distinguish the cross-sections of bineutron and single neutron emissions in the experiment.

For the combined $\sigma(\gamma, n) + \sigma(\gamma, pn)$ data, the peak is slightly lower and broader. The approximate fit parameters are $\sigma_{\max} \approx 170$ mb, $E_0 \approx 16.5$ MeV, and $\Gamma \approx 5.0$ MeV. The fitted cross section is:

$$\sigma(\gamma, n) + \sigma(\gamma, pn) \approx \frac{170}{1 + \left(\frac{E_\gamma^2 - 16.5^2}{5.0 E_\gamma}\right)^2} \quad \text{(mb)}.$$

The integrated cross section up to 25 MeV, accounting for the inclusion of the (γ, pn) channel and the broader width, is estimated as $\sigma_{\text{int}}(\gamma, n + \gamma, pn) \approx 1200$ to 1300 MeV·mb.

The higher integrated combined cross section is expected due to the additional (γ, pn) reaction channel and the increased resonance width.

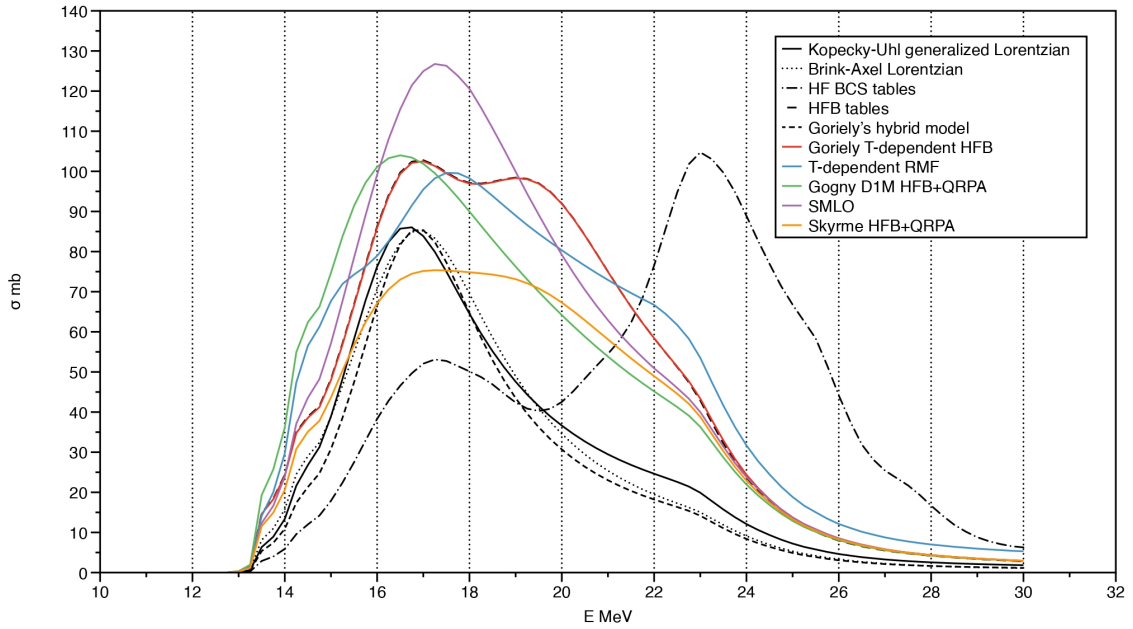

Figure 8: The calculation results of ^{92}Mo(γ, n) cross section by TALYS using deferent photon strength function, where solid black lines represent Kopecky-Uhl generalized Lorentzian model; dotted lines represent Brink-Axel Lorentzian model; dotted horizontal lines represent HF BCS tables model; long dashed lines represent HFB tables model; short dashed lines represent Goriely's hybrid model; red lines represent Goriely T-dependent HFB model; blue lines represent T-dependent RMF model; green line represent Gogny D1M HFB+QRPA model; purple lines represent SMLO model; and orange lines represent Skyrme HFB+QRPA model.

TALYS provides a comprehensive suite of models for photon strength functions (PSFs), which are crucial for predicting gamma-ray emission and absorption in nuclear reactions. These models range from phenomenological Lorentzian-based approaches to microscopic calculations grounded in mean-field theories. Below, we briefly introduce the ten implemented PSF options, focusing primarily on the dominant E1 mode while noting extensions to M1 where applicable.

1) Kopecky-Uhl Generalized Lorentzian (GLO)

The Generalized Lorentzian model, proposed by Kopecky and Uhl [18], adopts an energy- and temperature-dependent damping width to describe the E1 PSF. It is expressed as

$$f_{E1}(E_\gamma, T) = K_{E1}\left[\frac{E_\gamma \tilde{\Gamma}_{E1}(E_\gamma, T)}{(E_\gamma^2 - E_{E1}^2)^2 + E_\gamma^2 \tilde{\Gamma}_{E1}(E_\gamma, T)^2} + \frac{0.7\Gamma_{E1} 4\pi^2 T^2}{E_{E1}^5}\right]\sigma_{E1}\Gamma_{E1},$$

where $\tilde{\Gamma}_{E1}(E_\gamma, T) = \Gamma_{E1}(E_\gamma^2 + 4\pi^2 T^2)/E_{E1}^2$, and T is the nuclear temperature. This model ensures a non-zero limit at low energies and is suitable for radiative capture calculations.

2) Brink-Axel Lorentzian (SLO)

The Standard Lorentzian model, based on the Brink-Axel hypothesis [20], uses a simple Lorentzian form for the PSF:

$$f_{X\ell}(E_\gamma) = K_{X\ell}\frac{\sigma_{X\ell} E_\gamma \Gamma_{X\ell}^2}{(E_\gamma^2 - E_{X\ell}^2)^2 + E_\gamma^2 \Gamma_{X\ell}^2}.$$

It assumes no temperature dependence and is often applied to higher multipoles ($\ell > 1$) or as a baseline for M1 transitions.

3) HF BCS Tables

This model employs the spherical Hartree-Fock-BCS plus quasiparticle random-phase approximation (QRPA) based on the SLy4 Skyrme interaction [21]. The PSFs are tabulated, incorporating a folding procedure to account for damping effects. It provides E1 strengths for a wide range of nuclei, with phenomenological inclusion of deformation.

4) HFB Tables

An improved version of the previous model, this uses the spherical Hartree-Fock-Bogoliubov (HFB) plus QRPA framework with the BSk7 interaction [22]. It includes temperature-dependent corrections in the folding procedure, yielding energy- and temperature-dependent E1 PSF tables for over 8500 nuclei up to 200 MeV excitation energy.

5) Goriely's Hybrid Model

The hybrid model [23] combines elements of the GLO with a low-

energy behavior inspired by Fermi liquid theory:

$$f_{E1}(E_\gamma, T) = K_{E1}\sigma_{E1}\Gamma_{E1}\frac{E_\gamma\tilde{\Gamma}_{E1}(E_\gamma, T)}{(E_\gamma^2 - E_{E1}^2)^2 + E_\gamma^2\Gamma_{E1}\tilde{\Gamma}_{E1}(E_\gamma, T)},$$

where $\tilde{\Gamma}_{E1}(E_\gamma, T) = 0.7\Gamma_{E1}(E_\gamma^2 + 4\pi^2T^2)/(E_\gamma E_{E1})$. It ensures a non-zero low-energy limit and is useful for transitional regions.

6) Goriely T-dependent HFB

This temperature-dependent HFB plus QRPA model extends the Skyrme-based approach, providing tabulated E1 PSFs that account for the vanishing of deformation with increasing excitation energy. It is particularly suited for applications requiring thermal effects in the PSF.

7) T-dependent RMF

The temperature-dependent relativistic mean-field (RMF) plus QRPA model uses the PCF1 point-coupling force. It includes explicit continuum coupling and phenomenological corrections for complex configurations, temperature, and deformation, with tabulated E1 PSFs available in TALYS.

8) Gogny D1M HFB+QRPA

Based on the axially deformed HFB plus QRPA using the finite-range D1M Gogny force [24], this model provides both E1 and M1 PSFs. It includes a phenomenological low-energy M1 upbend and is validated against extensive experimental data, serving as a recommended microscopic option.

9) SMLO

The Simplified Modified Lorentzian (SMLO) model [25] offers an enhanced phenomenological description for E1 and M1 PSFs across $8 \leq Z \leq 124$:

$$\overleftarrow{f}_{M1}(\varepsilon_\gamma) = \frac{1}{3\pi^2\hbar^2c^2}\sum_i \frac{\sigma_i\varepsilon_\gamma\Gamma_i^2}{(\varepsilon_\gamma^2 - E_i^2)^2 + \varepsilon_\gamma^2\Gamma_i^2},$$

with parameters for spin-flip and scissors modes tuned to data. It includes temperature dependence and a low-energy upbend, making it the default phenomenological choice.

10) Skyrme HFB+QRPA

This encompasses the Skyrme-based HFB+QRPA calculations, providing microscopic E1 PSFs with temperature dependence. It accounts for quasiparticle collisions and is tabulated for broad nuclear coverage, emphasizing reliability for exotic nuclei.

6 Conclusions

The experimental data indicate a single-peak GDR structure with a resonance energy $E_0 \approx 16.5$ MeV, full width at half maximum (FWHM) $\Gamma \approx 3.5$ MeV, and peak cross section $\sigma_{\max} \approx 180$ mb for the (γ, n) channel, while the combined $(\gamma, n) + (\gamma, pn)$ channel exhibits a slightly lower peak ($\sigma_{\max} \approx 170$ mb) and broader width ($\Gamma \approx 5$ MeV). The calculations reveal distinct behaviors across the PSF models, which can be attributed to differences in their phenomenological or microscopic formulations.

The analysis of the ^{92}Mo(γ, n) reaction cross sections calculated using various photon strength function (PSF) models in TALYS reveals systematic discrepancies when compared to experimental data. The phenomenological models (1: Kopecky-Uhl GLO, 2: Brink-Axel SLO, 5: Goriely's hybrid, and 9: SMLO) yield resonance shapes that closely resemble the experimental single-peak GDR structure, with $E_0 \approx 16.5$ MeV and FWHM $\Gamma \approx 3.5$ MeV. However, these models consistently underestimate the peak cross section ($\sigma_{\max} \approx 90$ mb) relative to the experimental value of ≈ 180 mb and the TALYS-recommended GDR parameters ($E_{\max} = 16.82$ MeV, $\sigma_{\max} = 162$ mb, $\Gamma = 4.14$ MeV). This underestimation may stem from the global systematics employed in these Lorentzian-based approaches, which prioritize broad applicability across the nuclide chart but fail to capture nucleus-specific features such as local shell effects in ^{92}Mo (a near-magic $N = 50$ nucleus). At GDR energies, the dominant open channel is indeed (γ, n), with thresholds for additional channels like (γ, pn) lying higher; thus, the low predicted cross sections suggest potential inadequacies in the default PSF normalization or coupling to level densities, warranting parameter adjustments (e.g., scaling factors for height or width) to align with photoabsorption data.

In contrast, the microscopic models (3: HF-BCS tables, 4: HFB tables, 6: Goriely T-dependent HFB, 7: T-dependent RMF, 8: Gogny D1M HFB+QRPA, and 10: Skyrme HFB+QRPA) exhibit broader resonances ($\Gamma > 6$ MeV) and often multi-peak structures, particularly evident in models 3, 4, and 6 as double humps in the PSF data from TALYS gamma files (e.g., peaks at ≈ 17 MeV and $20 - 23$ MeV, with model 3 showing a dominant higher-energy peak). These features arise from QRPA calculations that incorporate residual interactions, pairing correlations, and deformation effects, leading to GDR splitting even in mildly deformed or transitional nuclei. The sharp drop-off around 23 MeV in these models could be attributed to the onset of competing channels (e.g., $(\gamma, 2n)$ or quasi-continuum transitions).

Overall, the microscopic PSFs deviate more significantly from the experimental single-peak profile, indicating that their ab initio nature, while theoretically robust, may overpredict structural complexity for ^{92}Mo due to assumptions in mean-field approximations or temperature dependencies.

In summary, phenomenological models offer superior shape fidelity but require empirical scaling to match absolute cross sections, whereas microscopic models provide insights into underlying nuclear structure but yield poorer agreement for this reaction, highlighting the need for hybrid approaches or refined inputs.

Bibliography

[1] F. R. Metzger, "Nuclear resonance fluorescence in as*sup*7*sup*5," *Physical Review (U.S.) Superseded in part by Phys. Rev. A, Phys. Rev. B: Solid State, Phys. Rev. C, and Phys. Rev. D*, vol. Vol: 110, 03 1958.

[2] M. Arnould and S. Goriely, "The p-process of stellar nucleosynthesis: astrophysics and nuclear physics status," *Physics Reports*, vol. 384, no. 1, pp. 1–84, 2003.

[3] A. Koning, S. Hilaire, and S. Goriely, "TALYS: modeling of nuclear reactions," *The European Physical Journal A*, vol. 59, p. 131, June 2023.

[4] F. A. Rasulova, N. V. Aksenov, S. I. Alekseev, S. S. Belyshev, I. Chuprakov, N. Y. Fursova, A. S. Madumarov, J. H. Khushvaktov, and A. A. Kuznetsov, "Photonuclear reactions on stable isotopes of molybdenum at bremsstrahlung endpoint energies of 10–23 mev," *Phys. Rev. C*, vol. 111, p. 024604, Feb 2025.

[5] J. Isaak, *Investigation of decay properties of the Pygmy Dipole Resonance and photon strength functions on excited states in (gamma, gamma' gamma") reactions.* PhD thesis, Mainz U., 2016.

[6] K. Heyde, P. von Neumann-Cosel, and A. Richter, "Magnetic dipole excitations in nuclei: Elementary modes of nucleonic motion," *Rev. Mod. Phys.*, vol. 82, pp. 2365–2419, Sep 2010.

[7] U. Kneissl, N. Pietralla, and A. Zilges, "Low-lying dipole modes in vibrational nuclei studied by photon scattering," *Journal of Physics G: Nuclear and Particle Physics*, vol. 32, p. R217, jun 2006.

[8] U. Kneissl, H. Pitz, and A. Zilges, "Investigation of nuclear structure by resonance fluorescence scattering," *Progress in Particle and Nuclear Physics*, vol. 37, pp. 349–433, 1996.

[9] A. Zilges, S. Volz, M. Babilon, T. Hartmann, P. Mohr, and K. Vogt, "Concentration of electric dipole strength below the neutron separation energy in n=82 nuclei," *Physics Letters B*, vol. 542, no. 1, pp. 43–48, 2002.

[10] H. R. Weller, M. W. Ahmed, H. Gao, W. Tornow, Y. K. Wu, M. Gai, and R. Miskimen, "Research opportunities at the upgraded his facility," *Progress in Particle and Nuclear Physics*, vol. 62, no. 1, pp. 257–303, 2009.

[11] A. P. Tonchev, S. L. Hammond, J. H. Kelley, E. Kwan, H. Lenske, G. Rusev, W. Tornow, and N. Tsoneva, "Spectral structure of the pygmy dipole resonance," *Phys. Rev. Lett.*, vol. 104, p. 072501, Feb 2010.

[12] E. Booth and K. A. Wright, "Nuclear resonance scattering of bremsstrahlung," *Nuclear Physics*, vol. 35, pp. 472–484, 1962.

[13] H. Utsunomiya, S. Goriely, H. Akimune, H. Harada, F. Kitatani, S. Goko, H. Toyokawa, K. Yamada, T. Kondo, O. Itoh, M. Kamata, T. Yamagata, Y.-W. Lui, I. Daoutidis, D. P. Arteaga, S. Hilaire, and A. J. Koning, "γ-ray strength function method and its application to ^{107}Pd," *Phys. Rev. C*, vol. 82, p. 064610, Dec 2010.

[14] J. Isaak, D. Savran, M. Fritzsche, D. Galaviz, T. Hartmann, S. Kamerdzhiev, J. H. Kelley, E. Kwan, N. Pietralla, C. Romig, G. Rusev, K. Sonnabend, A. P. Tonchev, W. Tornow, and A. Zilges, "Investigation of low-lying electric dipole strength in the semimagic nucleus ^{44}Ca," *Phys. Rev. C*, vol. 83, p. 034304, Mar 2011.

[15] S. Hilaire, M. Girod, S. Goriely, and A. J. Koning, "Temperature-dependent combinatorial level densities with the d1m gogny force," *Phys. Rev. C*, vol. 86, p. 064317, Dec 2012.

[16] H. Lan, T. Song, X. Huang, S. Zhao, J. Zhou, Z. Zhu, Y. Xu, D. L. Balabanski, and W. Luo, "Nuclear resonance fluorescence drug inspection," *Scientific Reports*, vol. 11, p. 1306, Jan. 2021.

[17] D. Habs and U. Köster, "Production of medical radioisotopes with high specific activity in photonuclear reactions with -beams of high intensity and large brilliance," *Applied Physics B*, vol. 103, pp. 501–519, May 2011.

[18] J. Kopecky and M. Uhl, "Test of gamma-ray strength functions in nuclear reaction model calculations," *Phys. Rev. C*, vol. 41, pp. 1941–1955, May 1990.

[19] T. Kawano, Y. Cho, P. Dimitriou, D. Filipescu, N. Iwamoto, V. Plujko, X. Tao, H. Utsunomiya, V. Varlamov, R. Xu, R. Capote, I. Gheorghe, O. Gorbachenko, Y. Jin, T. Renstrøm, M. Sin, K. Stopani, Y. Tian, G. Tveten, J. Wang, T. Belgya, R. Firestone, S. Goriely, J. Kopecky, M. Krtička, R. Schwengner, S. Siem, and M. Wiedeking, "Iaea photonuclear data library 2019," *Nuclear Data Sheets*, vol. 163, pp. 109–162, 2020.

[20] D. Brink, "Individual particle and collective aspects of the nuclear photoeffect," *Nuclear Physics*, vol. 4, pp. 215–220, 1957.

[21] S. Goriely and E. Khan, "Large-scale qrpa calculation of e1-strength and its impact on the neutron capture cross section," *Nuclear Physics A*, vol. 706, no. 1, pp. 217–232, 2002.

[22] I. Daoutidis and S. Goriely, "Large-scale Continuum Random Phase Approximation predictions of dipole strength for astrophysical applications," *Phys. Rev. C*, vol. 86, p. 034328, 2012.

[23] S. Goriely, "Radiative neutron captures by neutron-rich nuclei and the r-process nucleosynthesis," *Physics Letters B*, vol. 436, no. 1, pp. 10–18, 1998.

[24] S. Goriely, S. Hilaire, S. Péru, and K. Sieja, "Gogny-HFB+QRPA dipole strength function and its application to radiative nucleon capture cross section," *Phys. Rev. C*, vol. 98, no. 1, p. 014327, 2018.

[25] V. A. Plujko, O. M. Gorbachenko, R. Capote, and P. Dimitriou, "Giant Dipole Resonance Parameters of Ground-State Photoabsorption: Experimental Values with Uncertainties," *Atom. Data Nucl. Data Tabl.*, vol. 123-124, pp. 1–85, 2018.